Materials Today Communications 40 (2024) 109785

Contents lists available at ScienceDirect

Materials Today Communications

journal homepage: www.elsevier.com/locate/mtcomm

Mechano-bactericidal activity of two-photon polymerized micro-and nanoscale topographies against *Pseudomonas aeruginosa*: Surface interactions and antibacterial efficacy

Ning Tan [a,b,*], Jisun Im [c], Nigel Neate [d], Chee-Onn Leong [e], Ricky D. Wildman [c], Georgina Elizabeth Marsh [b,f,g], Maxine Swee-Li Yee [b,**]

[a] Department of Mechanical, Materials & Manufacturing Engineering, University of Nottingham Malaysia, Malaysia
[b] Nanotechnology Research Group, Center for Nanotechnology and Advanced Materials, University of Nottingham Malaysia, Malaysia
[c] Centre for Additive Manufacturing, University of Nottingham, United Kingdom
[d] Nanoscale and Microscale Research, University of Nottingham, United Kingdom
[e] AGTC Genomics, J2-1 Pusat Perdagangan Bandar, Persiaran Jalil 1, Bukit Jalil, Kuala Lumpur 57000, Malaysia
[f] School of Pharmacy, University of Nottingham Malaysia, Malaysia
[g] Pharmacy, Swansea University Medical School, Singleton Park, Swansea University, United Kingdom

ARTICLE INFO

Keywords:
Bactericidal
Synthetic micro-/nano-topography
Two-photon polymerization
Antibacterial surface

ABSTRACT

The emergence of antimicrobial-resistant bacteria poses a significant health concern, stemming from chemically induced intrinsic and acquired-resistance responses in the microbe. Nanopatterns are an alternative bactericidal approach, employing physical features to prevent biofilm formation and kill bacteria. This work draws inspiration from the natural mechano-bactericidal properties of sub-micron scale surface structures present on cicada wings, with the fabrication of synthetic, chemically-inert surfaces using the two-photon polymerization (2PP) technique. In contrast to the random packing and distribution of the nanotopography of cicada wings, the 2PP synthetic surfaces were produced with highly uniform and precise surface geometries of nanopillars and micropillars. These synthetic topographies with hexagonal-arranged nano/micro features induced a spacing-dependent response in *Pseudomonas aeruginosa*, influencing their cell viability, adhesion property and biofilm formation ability. Optimized spacings ~500 nm between nanopillars were associated with higher proportions of distorted and ruptured bacteria cells, while up to 60 % reduction of biofilms were observed on micropillared surfaces with ~2 micron spacings between pillars. Whole transcriptome analysis of bacteria exposed to the synthetic surface indicated significant upregulation of a single pathway associated with quorum sensing. The PA3305.1 pathway induced quinolone signal synthesis in *P. aeruginosa*. The findings of this study establish the basis for developing complex antimicrobial surfaces using a physical approach, without reliance on chemical means.

1. Introduction

As bacteria exhibit the ability to colonize a wide array of surfaces, both abiotic and biotic, such as medical devices, implants, and host tissues, they form biofilms consisting of surface-attached colonies encased within an extracellular matrix (ECM) produced by the bacteria [1]. This matrix composed of nucleic acids, polysaccharides and proteins, acts as a formidable barrier against antibiotics, environmental stresses, and immune responses, thereby promoting resistance to antimicrobials [2,3]. Biofilm-associated infections account for a substantial portion of microbial diseases, with bacterial biofilms contributing to approximately 80 % of chronic infections, as reported by the National Institutes of Health (NIH) [1]. The propensity for biofilm formation on implant surfaces in healthcare settings is a major contributor to implant-associated infections (IAI), and this problem is exacerbated by the growing number of patients receiving biomedical implants [4]. Knee replacement surgeries, for instance, have seen a 35 % increase between 2009 and 2019 [4]. The prevalence of IAI, often caused by

* Corresponding author at: Department of Mechanical, Materials & Manufacturing Engineering, University of Nottingham Malaysia, Malaysia.
** Corresponding author.
E-mail addresses: hbynt1@nottingham.edu.my, tanning7@gmail.com (N. Tan), Maxine.Yee@nottingham.edu.my (M.S.-L. Yee).

https://doi.org/10.1016/j.mtcomm.2024.109785
Received 30 December 2023; Received in revised form 3 June 2024; Accepted 6 July 2024
Available online 8 July 2024

pathogens such as *Pseudomonas aeruginosa*, *Staphylococcus aureus*, and *Staphylococcus epidermidis* [5,6], necessitates prolonged antibiotic administration and surgical interventions [7], incurring significant social and financial burdens [8]. Conventional treatment of IAI with antibiotic coatings often lacks efficacy due to two major traits of bacteria: (1) their ability to form biofilms that subsequently damage the surface and functionality of biomaterials, and (2) their adaptability which give rise to the evolution of antibiotic resistance. Chemical-based antimicrobial strategies face limitations, including potential toxicity, temporal depletion of antimicrobial agents, and the emergence of antibiotic resistant microbial strains [9–11]. In this context, the non-chemical approach presented in this study seeks to inhibit bacterial cell formation and proliferation on surfaces, in order to address the challenges posed by antimicrobial-resistant bacteria.

Researchers exploring natural surfaces with inherent antibacterial properties have focused on the evolutionary defence mechanisms developed by various organisms to counteract bacterial colonization. Notably, the nano topographical features with a high aspect ratio found on the wings of cicadas (Fig. 1a) and dragonflies have demonstrated remarkable mechano-bactericidal activity [11,12]. The wing surface of the cicada species *Psaltoda claripennis* exhibits bactericidal properties against *P. aeruginosa*. The observed effect is solely attributed to the nanostructure, independent of any chemical interaction with the surface [13]. The underlying physical principle involves the application of deforming stress by nanotopographies to surface-adhered bacterial cells. Nature's ingenious designs have inspired the development of biomimetic antibacterial surfaces capable of exhibiting both bactericidal and anti-biofouling characteristics. The riblet microtopography on shark skin acknowledged as an early example of biomimicry in engineering antifouling properties [14], incorporates small grooves between the riblets that discourage the settlement of microorganisms and promote low adhesion [15]. A slippery liquid-infused microstructured surface inspired by the *Nepenthes* pitcher plants demonstrated efficacy in preventing the attachment of *P. aeruginosa* biofilm, as well as inhibiting *S. aureus* and *E. coli* over a 7-day period [16].

To create surface topographies that are highly effective against infections, it is crucial to employ a technique with superior design control and 3D structure capability, negating the reliance on chemical-based antimicrobials. Traditional lithographic methods are restricted to 2D structures, rendering them incapable of creating true 3D structures with high aspect ratios [17]. Various techniques, such as two-photon polymerization (2PP), X-ray lithography, and electron beam lithography can be utilized to fabricate micro- and nano-topographies for *in vitro* studies. In recent times, there has been a growing interest in utilizing the 2PP direct laser writing technique for the fabrication of microfluidic devices, biomedical implants, and bio-inspired architectures [18]. The high precision and 3D fabrication capability of 2PP position it as the most promising method for developing precise micro-/nanostructured surfaces in the context of this study.

In a typical 2PP process, a near-infrared (NIR) femtosecond laser beam ($\lambda = 780$ nm) is focused through a high numerical aperture (NA) objective lens into a photopolymer resin (IP-L 780) that is composed of reactive oligomers and a photoinitiator (Fig. 1b). Polymerization occurs when two or more photons are absorbed simultaneously and at the region where the light intensity reaches the threshold for polymerization. Polymerization is confined within the focal volume of the resin, utilizing the NIR laser to tightly focus onto a spot through a spatial and temporal Gaussian pulse to form the smallest building block of the 3D structure, known as a voxel, providing an extremely localised effect and high resolution structures [18]. The scanning movement of the laser focus can be realised in two ways: (1) the galvo scanner moves in x- and y-axes while the sample is moved along the z-axis or (2) by using a 3D piezo

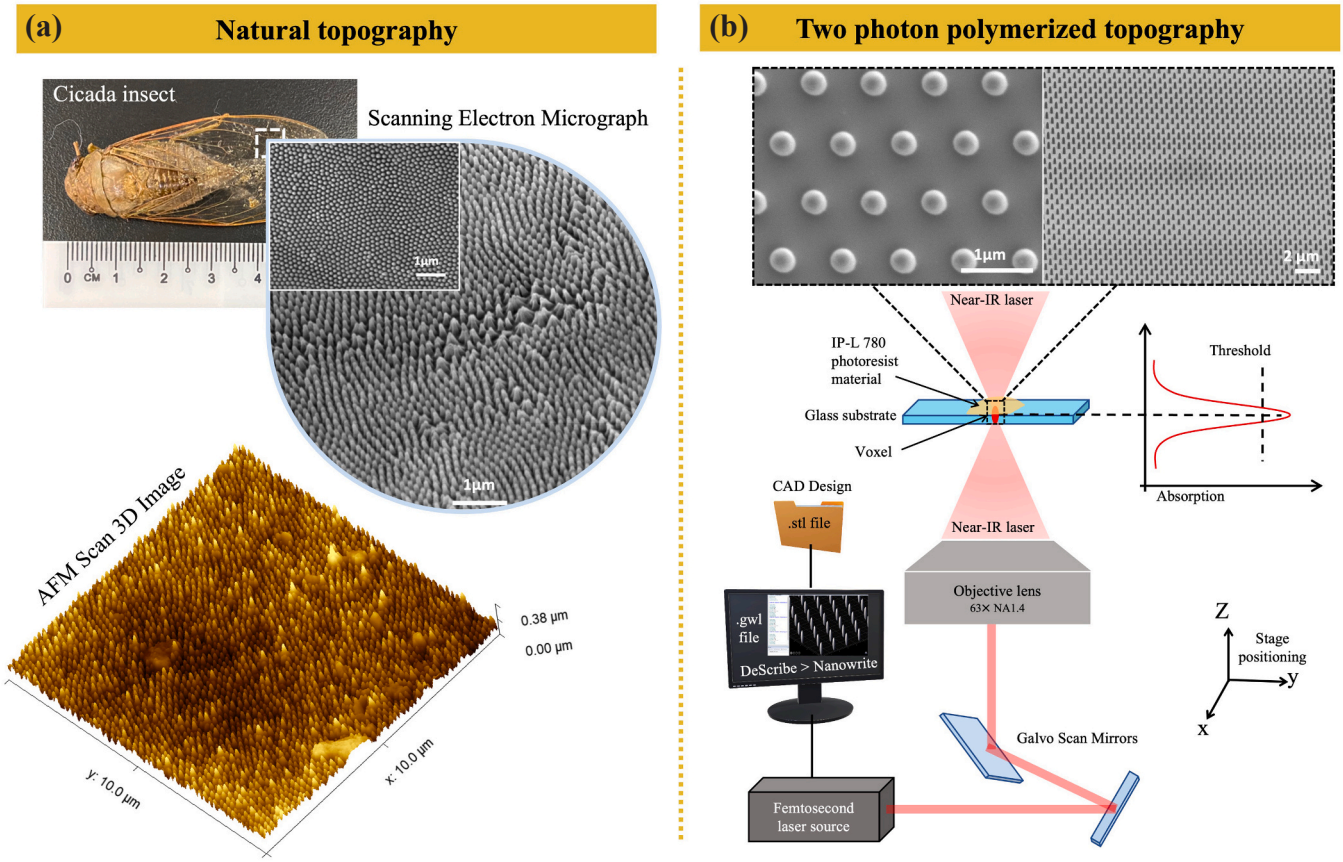

Fig. 1. Comparison between (a) the natural topography of a cicada wing and; (b) the biomimetic nanotopography fabricated through simultaneous two-photon polymerisation of the IP-L 780 photoresist loaded on a glass substrate.

stage to move in three dimensions [19]. The transparency in the NIR spectral band allows greater optical penetration depth of laser pulses in the photoresist volume, forming true 3D structures through the stacking of polymerized voxels without requiring a photomask [17]. Further details revolving around the sub-processes of the 2PP photopolymerization has been discussed previously [19].

The primary goal of this research is to draw inspiration from the natural mechano-bactericidal properties inherent in sub-micron scale surface structures observed on cicada wings. The focus lies on replicating these properties through the fabrication of synthetic surfaces using 2PP. Specifically, the aim is to engineer chemically-inert surfaces that mimic the intricate structures found on cicada wings, leveraging the precision offered by 2PP for the creation of micro- and nanoscale topographies. Through this approach, the research seeks to achieve synthetic surfaces with mechano-antibacterial capabilities, with potential applications in healthcare and industry where addressing bacterial infections is a critical objective.

2. Materials and methods

2.1. Preparation of natural nanostructured surface from cicada wing

Cicada specimens were purchased online (etsy.com) and visually identified as *Dundubia vaginata*. An incision of approximately 0.5 cm×0.5 cm was made on the forewings of the cicada using scissors. The excised wings were subsequently attached to a 22 mm×22 mm glass coverslip by a double-sided adhesive tape. The wings were briefly rinsed with 70 % isopropyl alcohol (IPA) followed by autoclaved distilled water and finally left in the biosafety cabinet to air dry for several hours.

2.2. Fabrication of synthetic microstructured surfaces and nanostructured surfaces

2.2.1. 3D Print

The herein presented structures have been fabricated with the Photonic Professional GT 3D printer (Nanoscribe GmbH, Germany). The key 3D printer fabrication parameters have been discussed in our previous work [20]. All structures in this study were printed using the commercially available liquid photoresist, IP-L 780 (Nanoscribe GmbH, Germany) that is composed of >95 % 2-(Hydroxymethyl)-2-[[(1-oxoallyl) oxy]methyl]-1.3-propanediyl diacrylate and <5 % 7-(Diethylamino)-3-(2-thienylcarbonyl)-2 H-1-benzopyran 2-one. The system used a Ti: Sapphire laser emitting 100 fs pulses at 780 nm in the near-infrared spectrum. The laser beam was focused using an oil immersion objective lens (63x NA 1.4). All structures were printed on 22 mm × 22 mm glass substrates (high precision microscope cover glass, No. 1.5 H, Marienfeld, Germany).

2.2.2. Computer-aided design (CAD)

Prior to fabrication via 2PP, the micro and nanogeometries were designed using 3D CAD software (Blender 3.2.2, the Netherlands). Micropillar arrays with two different inter-pillar centre-to-centre spacing values of 5 μm and 8 μm were designed. Each micropillar in the arrays have a diameter of 3 μm and a height of 4.5 μm. Subsequently, the associated stereolithography (STL) file generated from Blender were processed by a proprietary DeScribe software (Version 2.5.7, Nanoscribe GmbH, Germany) and was imported directly to the Nanoscribe system in general writing language (GWL) format to print. Similarly, several nanopillar arrays with inter-pillar centre-to-centre spacing values of 700 nm, 800 nm, 1000 nm, 1500 nm, and 2000 nm were defined using the continuous mode of the DeScribe software.

2.2.3. Fabrication via two-photon polymerisation (2PP)

Arrays of micropillars and nanopillars were printed over an area of 300 μm x 300 μm by 2PP using the 3D printer. A drop of IP-L 780 was drop-cast on the glass substrate and subsequently mounted onto the predefined position of the sample holder, the holder was then inverted and a drop of immersol 518 F immersion oil (Nanoscribe GmbH, Germany) was drop-cast on the underside of the substrate for refractive index contrast. The samples were developed in propylene glycol monomethyl ether acetate (PGMEA ≥ 99.5 %) (SigmaAldrich, USA) for 30 minutes followed by isopropanol (≥ 99.9 %) (SigmaAldrich, USA) for five minutes, to wash away excess liquid 2PP resin, before drying with compressed air.

2.3. Morphological observations of natural and synthetic topographies

2.3.1. Scanning electron microscopy (SEM)

Samples were affixed on a metal stub with copper tape and sputter coated with ~6 nm gold. High-resolution electron micrographs of the morphology and the cross-section of the micro- and nanopillar surfaces were characterised by a field emission gun scanning electron microscope (FEG-SEM, 7100 F, JEOL, Japan), acquired using a probe current of 10 μA at 1 kV. The height of the printed structures was analysed from the SEM image through the cross-sectional view obtained via a 60° tilt. ImageJ software was used to measure the distance between the centre of each neighbouring pillar (centre-to-centre spacing) and diameter of the pillars. SEM images were obtained from three separate samples, with at least three independent fields containing over 20 pillars in each field.

2.3.2. Atomic force microscopy (AFM)

The topographical features of the nanopillar arrays, including height and centre-to-centre spacings, were further characterized using a Bruker Dimension Icon Atomic Force Microscope (Bruker, USA) in the PeakForce (PF) Quantitative Nanomechanics (QNM) tapping mode, at ambient temperature over a scan area of 10 μm x 10 μm, with scan frequency of between 0.3 and 0.5 Hz. An antimony (n) doped Si probe (Bruker tip model: RTESPA-150) with a cantilever width of 35 μm, length 125 μm, and thickness of 1.25 μm, a nominal spring constant of 6 N/m, and resonance frequency of 150 kHz was used. All AFM scans were post-processed using Gwyddion 2.6, to obtain the mean heights and spacings of the pillars, as detailed in our previous work [20].

2.3.3. Optical profilometry

Surface analysis of the microtopography was carried out using the Profilm3D®, Optical profilometer (Filmetrics, USA). Optical micrographs were captured using a 50X Nikon DI objective. Topographic scans for each sample were processed using the Profilm3D software version 3.5.6.2.

2.4. Bacterial cell interaction assays

Common bacterial cells responsible for biofilm formation, Gram-negative *P. aeruginosa* ATCC 27853, purchased from the American Type Culture Collection (ATCC), was used in this study. Before each experiment, stock bacterial cultures were refreshed on nutrient agar (Oxoid Ltd, United Kingdom). Fresh bacterial suspensions were cultured overnight at 37 °C in 5 mL of Luria Bertani (LB) broth (HiMedia, Mumbai, India). Bacterial cells were collected at the exponential phase and the density of the bacterial suspension was adjusted using the same growth media to OD_{600}= 0.1 using UV–visible spectrophotometry (Biochrom Libra S12, United Kingdom), followed by a 10,000-fold dilution to ensure consistent assays for all samples. Microstructured and nanostructured surfaces were covered in 15 μL of the adjusted bacterial suspension and incubated at 37 °C for 24 hours. A flat glass coverslip without any 3D print was used as the control surface.

2.4.1. Cell viability and adhesion analysis

To assess the viability of bacteria adhered to nanopillared surfaces, the LIVE/DEAD™ BacLight™ Bacterial Viability Kit (Invitrogen, Thermo Fisher Scientific, USA) was employed. Prior to staining with the LIVE/DEAD staining solution, samples were washed twice with 0.85 %

sodium chloride (NaCl) (Systerm Chemicals, Malaysia) solution at room temperature by streaming the NaCl alongside the sample and gently swirling the plate, to remove significant traces of interfering culture media from the sample surface. The LIVE/DEAD staining solution was prepared by mixing the two stains (SYTO9 and propidium iodide (PI)) at a 1:1 ratio with 0.85 % NaCl buffer as recommended by the manufacturer, followed by incubation of the sample with 15 μL of the staining solution in the dark at room temperature for 15 min [21]. The stained sample was then imaged by ZEISS Colibri 7 fluorescence microscopy (ZEISS, Germany) with emission wavelengths of 530 nm for SYTO9 and 645 nm for PI. The number of live cells (labelled green by SYTO9) and dead cells (labelled red by PI) on the nanopillared surfaces of each fluorescence micrograph were counted using Fiji image processing software and plotted as the percentage of live cells to dead cells. Each sample contained a minimum of 200 cells. The percentage of dead cells on the surface was calculated using the equation:

$$\text{Percentage of dead cells}\,(\%) = \frac{\text{Number of surface attached dead cells}}{\text{Total number of surface attached cells}} \times 100$$

2.4.2. Static biofouling analysis

The anti-biofouling activity of micropillared surfaces was assessed using crystal violet (CV) assay and compared to the control. The samples were stained with 0.1 % (v/v) CV solution (Merck, USA) for 15 min. Excess CV was then removed, and samples were gently rinsed twice and air dried. This was followed by the addition of 30 % acetic acid (Chemiz, Malaysia) to dissolve the cell-bound CV. Biofilm growth was monitored in terms of the CV optical density at 550 nm (OD_{550}) using the Epoch microplate reader (BioTek® Instruments, USA). All data are expressed as mean ± standard deviation (SD) of the triplicate experimental data. The percentage biofilm on micropillared surfaces with respect to control was calculated using the equation:

$$\text{Percentage Biofilm} = \frac{\text{Surface Type } OD_{550}}{\text{Mean Control Flat } OD_{550}} \times 100$$

2.4.3. Bacterial cell morphology analysis

Bacterial morphology exposed to nanopillared surfaces was examined using FEG-SEM. The samples were fixed with 4 % paraformaldehyde (Sigma-Aldrich, USA) for 30 minutes, followed by a series of dehydration steps. Briefly, dehydration was carried out by immersing the samples in ethanol (R&M Chemicals, Malaysia) and water mixtures with increasing concentrations (50 %, 60 %, 70 %, 80 % and 99.8 %). The samples were then dried in a fume hood using increasing ratios of hexamethyldisilazane (HMDS) solution (Thermo Scientific, Waltham, USA) to ethanol, starting from a ratio of 1:2, 2:1 and finally pure HMDS.

2.5. Whole transcriptome sequencing and analysis

The *P. aeruginosa* strain was grown overnight in LB medium at 37 °C, and the cultures were subsequently diluted to OD_{600} of 0.1. Diluted cultures were incubated on the synthetic nanopillared surface SP 800 (with flat glass coverslip without 3D print as the control surface) for 24 hours. For transcriptomic analysis, RNA was extracted with TRIzol (Invitrogen, USA) according to the manufacturer's protocol and purified using QIAGEN RNAeasy Clean-up Kit (QIAGEN, Germany). The purity and concentration of RNA samples were evaluated using an Implen NanoPhotometer (Implen, Germany) and Invitrogen Qubit 4 fluorometer (Invitrogen, USA), respectively. The Illumina® Stranded Total RNA Prep, Ligation with Ribo-Zero Plus kit (Illumina, USA) was used to generate the cDNA library, according to the manufacturer's instructions. After adapter ligation, 16 cycles of PCR amplification were performed. Constructed libraries were quantified using the LabChip® GX Touch™ nucleic acid analyzer (Revvity, USA). The Illumina NovaSeq 6000 System (Illumina, USA) was used for sequencing to generate 76-bp paired-end reads. Demultiplexing of samples was performed using Illumina DRAGEN Bio-IT Platform v3.9 (Illumina, USA). Data normalization and quantification were done using Salmon, an R package. Reference database (.fasta) and Gene transfer format (GTF) used in R were downloaded from the NCBI database. Differential expressed genes (DEG) were identified using the R package, DESeq2, while explorations of different molecular mechanisms and involved pathways were performed with the R package, clusterProfiler.

2.6. Statistical analysis

Statistical analysis using Student's t-test was done to verify the statistical significance of biofilm formation across the micropillared samples compared to biofilm formed on flat control surfaces. A significance threshold of $P < 0.05$ was applied. Statistical evaluations were performed with the IBM SPSS Version 29.0.2 software. All experimental procedures were performed in biological triplicates (n=3).

3. Results and discussions

3.1. Natural topography of cicada wing

An AFM scan of the cicada forewing sample revealed a densely packed nanotopography with disordered hexagonal arrangement consisting of nanopillars with irregular heights (Fig. 2a). The nanopillars are composed of 2 parts: a curvilinear base connected to a cylindrical top, forming a tapered geometry. These pillars ranged in spacing from 150 to 380 nm and exhibited a height distribution of 130–330 nm. ImageJ analysis revealed significant variability in the dimensions of the pillar structures within individual samples of cicada wings. The centre-to-centre spacings averaged 234 ± 133 nm, while the heights were approximately 278 ± 91 nm. The base diameter was approximately 130 nm. The substantial standard deviations across these measurements indicate considerable variation in the nanopillar geometry on cicada wings.

3.2. Antibacterial property of natural topography on cicada wing

The bactericidal activity of the cicada wing nanotopography was quantitatively evaluated over a 24-hour incubation period using LIVE/DEAD™ staining. The staining solution contains two nucleic acid stains: SYTO9 and PI. Healthy cells exposed to the solution will fluoresce green due to the SYTO9 stain, while cells with compromised membranes will fluoresce red due to the permeation of PI. Early data points from the LIVE/DEAD cell count on the cicada wing were excluded because the bacterial cells on the surface were too densely populated. These cells formed aggregates that could not be precisely quantified using the FIJI image processing software. The uneven distribution of live and dead cells across the tested cicada wing surface (Fig. 2b) indicated suboptimal killing efficiency. A substantial proportion of viable cells was found across most parts of the wings, while non-viable cells were concentrated in localized regions.

In addition to the fluorescence imaging, the changes in bacterial cell morphology resulting from the nanotopographical features of the cicada wing were investigated. The majority of the *P. aeruginosa* cells attached to the cicada wing surface did not exhibit any significant difference in their cell morphology. A few cells adhering to the cicada wing were seen as deflated and pierced by the nanopillars (Fig. 2c) which corroborates with the LIVE/DEAD results. These observations suggest that the tapered nanopillar geometry on the cicada wings inflicts a certain degree of disruption to the surface-attached bacteria cells as described by Kelleher [12]. The disrupted bacterial cells on the cicada wing are consistent with previous studies whereby the *P. aeruginosa* strain showed initial stretching and consequently inactivation of bacterial cells after incubation with the wings of *P. claripennis* cicada [22].

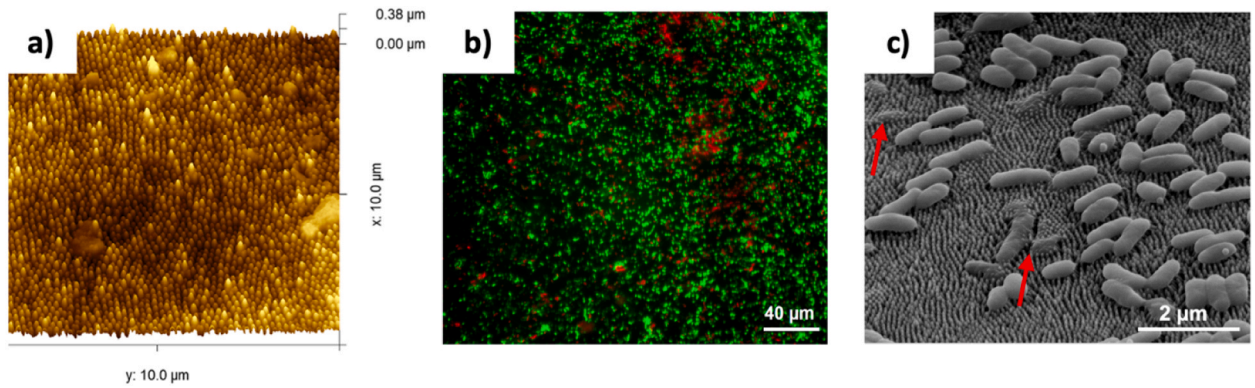

Fig. 2. (a) Atomic force microscopy (AFM) image of Dundubia vaginata cicada wing revealing considerable variation in the natural nanopillar geometry, (b) fluorescence microscopy image of Pseudomonas aeruginosa stained with SYTO9/PI on cicada wing sample, (c) cross-section view of the scanning electron microscope (SEM) image of Pseudomonas aeruginosa attached on the surface of cicada wing, captured at x 30,000. The red arrows indicate a few cells pierced and deflated by the natural nanopillars of the wing structure.

Recent studies have reported an association between the mechanical bactericidal mechanism and nanopillars, which induces cell membrane rupture and deformation, resulting in flattened cell morphology in the scanning electron micrograph [11]. According to the proposed stretching model, the bactericidal mechanism is attributed to the stretching effect caused by the adsorption of bacterial cell walls onto the cicada wing nanotopography. This model is based on increased adsorption, leading to irreparable cell membrane rupture and eventually bacterial death. If the stretching degree of the cell membrane exceeds its threshold, it would lead to mechanical ruptures in bacterial cell walls [23]. On the other hand, highly dense packing of the rigid pillars was found to counteract the force exerted on the bacterial membrane, thereby limiting the extent to which the bacterial cell could stretch and thus, reducing the bactericidal effect [11]. An alternative proposed model known as the “ripping model” aims to elucidate the mechanism behind the death of *E.coli* caused by the uneven nanopillars on dragonfly wings. According to this model, the shear forces generated by the movement of cells attached to the nanopillars result in the ’ripping’ of bacterial membranes [12]. Thus, the irregular spacing of nanostructures on cicada wings can explain the uneven distribution of live and dead cells observed in Fig. 2(b). Therefore, our subsequent work focused on utilizing the 2PP technique to fabricate nano-/microstructure topography with precise, controlled geometry and spacing, aiming to enhance the antibacterial efficiency.

3.3. Synthetic nanotopography and microtopography from two-photon polymerization

3.3.1. Nanotopographies

The AFM scans shown in Fig. 3(a)-(e) show nanopillars fabricated through 2PP based on the CAD model design. These nanopillar arrays were designed in an orderly hexagonal arrangement to exhibit a fixed interpillar centre-to-centre spacing ranging from 700 nm (labelled as sample SP 700) to 2000 nm (labelled as sample SP 2000). Table 1

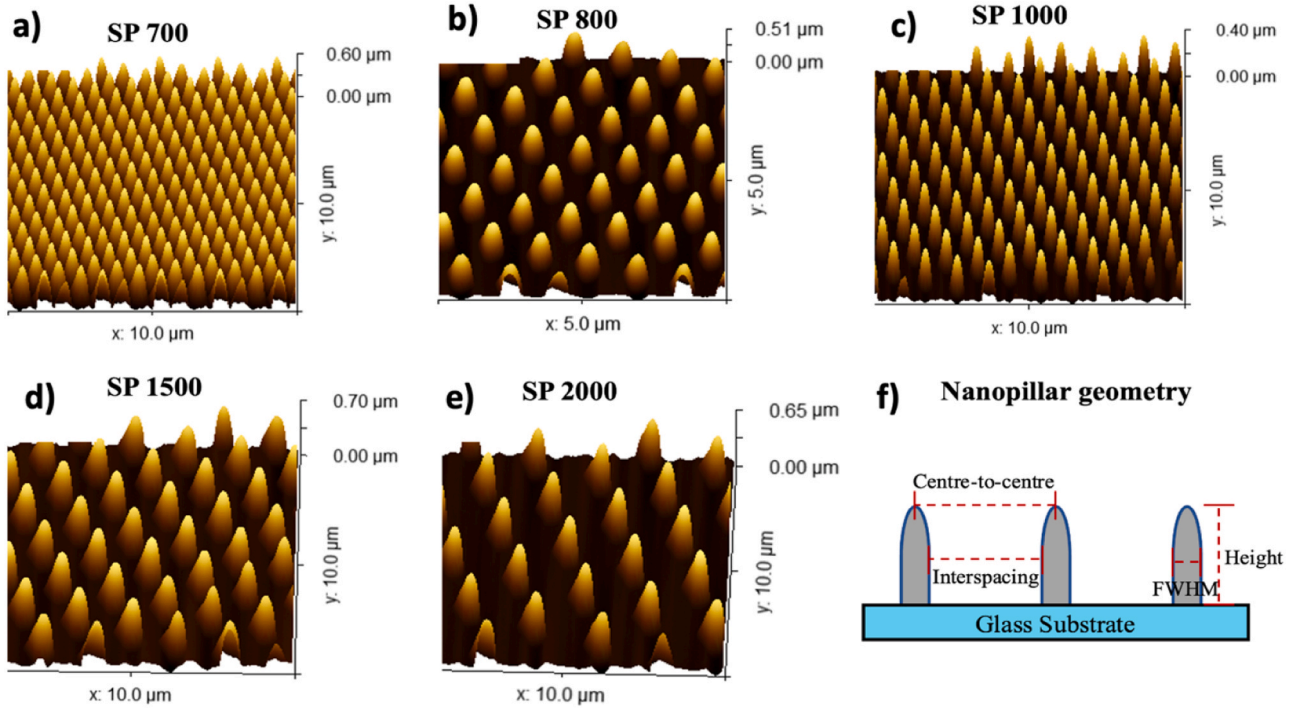

Fig. 3. (a)-(e) Three-dimensional view of AFM scan of 2PP nanopillar sample with varying centre-to-centre spacings, (f) Schematic of nanopillar geometrical measurement. FWHM= full-width half maximum.

Table 1
Measured parameter of 2PP printed nanopillar arrays.

Sample	2PP nanopillar arrays				
	SP 700	SP 800	SP 1000	SP 1500	SP 2000
Centre-to-centre spacings [nm]	726 ± 34	816 ± 42	1056 ± 46	1586 ± 70	2153 ± 95
FWHM [nm]	359 ± 44	315 ± 31	318 ± 28	383 ± 30	372 ± 30
Heights [nm]	590 ± 8	490 ± 14	380 ± 14	680 ± 21	630 ± 24
Aspect Ratio	0.61 ± 0.08	0.64 ± 0.05	0.83 ± 0.04	0.56 ± 0.03	0.59 ± 0.03
Interspacing [nm]	367 ± 49	501 ± 32	738 ± 27	1203 ± 34	1781 ± 34

NOTE: FWHM represents the width measured at full-width half maximum of the nanopillar. Spacings and height values are represented as mean ± standard deviation (s.d.). Aspect ratio = FWHM/ Height. Mean interspacing = mean centre-to-centre spacings – mean FWHM.

presents the mean dimensional data for these nanopillar arrays, including centre-to-centre spacing, height, full width at half maximum (FWHM), aspect ratio, and interspacing. Interspacing refers to the gap between the walls of adjacent pillars, as depicted in Fig. 3(f).

Interestingly, standard deviation values of centre-to-centre spacings below 5.2 % within each sample group (Table 1) in 2PP nanopillars indicate greater controllability of the spacings via 2PP fabrication as compared to the natural topography found on cicada wings, thus enhancing the overall homogeneity of the nano topographical surface. With the controllability and precision of 2PP to produce geometrically uniform nanopillar arrays, it is possible to investigate the effect of centre-to-centre spacing on the bactericidal activity of the 2PP nanopillared surfaces.

The heights of the nanopillar arrays, analysed from AFM scan measurements, were found to range between 380 nm – 680 nm. The width of the nanopillars, ranging between 315 nm – 383 nm, represented by the Full Width at Half Maximum (FWHM) in Fig. 3(f), was used to calculate the nanopillar aspect ratio (Width/ Height). The aspect ratio, ranging from 0.56 – 0.83, was then assessed to determine its influence on bactericidal efficacy.

A few studies have investigated the relationship between nanostructure height and bactericidal efficacy against Gram-negative bacteria. Dickson [24] et al. reported that height was not a critical factor in enhancing bacterial killing efficiency, PMMA nanopatterned surfaces of the same height (300 nm) but different feature spacings showed increases of bactericidal effect on *E.coli* cells between 16 % and 97 % for spacings between 380 nm and 130 nm, respectively, when compared with flat controls. Dickson's result implied that smaller and more closely spaced pillars have a greater bactericidal effect. Another study also reported no direct correlation between nanofeature heights and bactericidal activity against *E. coli* and *K. pneumoniae* bacterial cells [25]. Notably, the sinking rate of *P. aeruginosa* cells onto the nanopillars was tracked using a point force microscope, it was reported that the rod-shaped bacteria cells slowly moved downwards by approximately 200 nm before an abrupt downward motion resulting in the membrane rupture point, implying that ~200 nm could be the "critical" height needed to induce membrane rupture [26]. Therefore, the height of the fabricated nanopillar was capped within the bactericidal height range (~300–600 nm).

Other factors such as the centre-to-centre spacings and pattern arrangement were evaluated in the present study as they could influence the bactericidal efficacy. The selected centre-to-centre spacing in this study encompasses a wide range of interspaces, including those greater than previously reported values. It is worth noting that effective bactericidal interspaces are dependent on the type of bacterial strains and their attachment to the surfaces [27]. The comparatively thinner peptidoglycan layer of gram-negative *P. aeruginosa* than gram-positive bacterial cells poses more vulnerability to its rapid cell death [28].

Hence, for our preliminary study, we have chosen *P. aeruginosa* as a model bacterium to show proof-of-concept of 2PP fabricated nanopillars exhibiting bactericidal activity through mechanical damage. The model bacterium used in this study has a typical dimension of approximately 1–5 μm length and 0.5–1.0 μm diameter [29]. Bacterial cells would adopt orientations to position themselves between the nanopillars of greater interspaces (interspacing > bacterial cell diameter), by way of circumventing the interaction with the nanopillars [30]. The arrangement of the nanostructures was also found to significantly affect the attachment behaviour of bacterial cells to the surface. Nanopatterns having a regular square arrangement were reported to produce slightly larger sinking depths and lower envelope stresses on bacterial cells than those with hexagonal ordering. According to Amar et al. [30], the trend in bacteria-killing efficiency has a positive correlation with the theoretical maximum von Mises stress. It was reported that the hexagonally ordered nanopattern produced a higher maximum von Mises stress than the square arrangement due to the selective reduction in nanopillar centre spacing in hexagonal patterns [30].

Therefore, the hexagonal arrangement of nanopillars was adopted in our study to enhance the stress exerted on the cell envelope and achieve the selective reduction in the relative diagonal spacings (standardize the relative spacings within the nanopattern) of the pillar. This work primarily studies the effect of various nanopillar spacings achieved through 2PP and its bactericidal efficacy.

3.3.2. *Microtopographies*

Two distinct micropillar arrays with hexagonal pillar arrangements were fabricated using 2PP. These arrays consisted of micropillars with centre-to-centre spacings of 5 μm and 8 μm respectively. The micropillar heights of both arrays were approximately 4–5 μm and pillar width of 2.8 μm, as measured with 3D profiling instrument. The micropillar array with 8 μm centre-to-centre spacings had interspaces of ~ 5 μm, while the array with 5 μm spacings had interspaces of ~ 2 μm. These microtopographies were then assessed for their effect on inhibiting biofilm formation by *P. aeruginosa*.

3.4. *Antibacterial activity of nanostructured and microstructured topographies*

3.4.1. *Effect of pillar spacings in nanopillar arrays on antibacterial activity*

The fluorescent micrographs and the corresponding SEM images of nanopillars after being incubated for 24 hours with *P. aeruginosa* is shown in Fig. 4(a)-(f). From fluorescence imaging, we can observe the changes in bacteria viability when exposed to nanopillar arrays with different spacings. Significant proportions of red labelled bacterial cells were observed on SP 2000 (Fig. 4a), SP 1500 (Fig. 4b) and SP 800 (Fig. 4d), while a major proportion of bacteria appeared with the green label on SP 700 (Fig. 4e), SP 1000 (Fig. 4c) and the flat control (Fig. 4f). This indicates low bactericidal activity notably on the flat control, SP 700 and SP 1000 nanopillar array.

Furthermore, some webbed structure was observed on SEM images, such as in Fig. 4(c) and Fig. 4(d). The webbing could indicate the presence of extracellular polymeric substances (EPS) indicating the bacterial interaction with the nanopillar surface. In addition, aggregations of bacterial cells were observed in Fig. 4(f). As noted in the fluorescence image of Fig. 4(c), SP1000 showed the highest proportion of

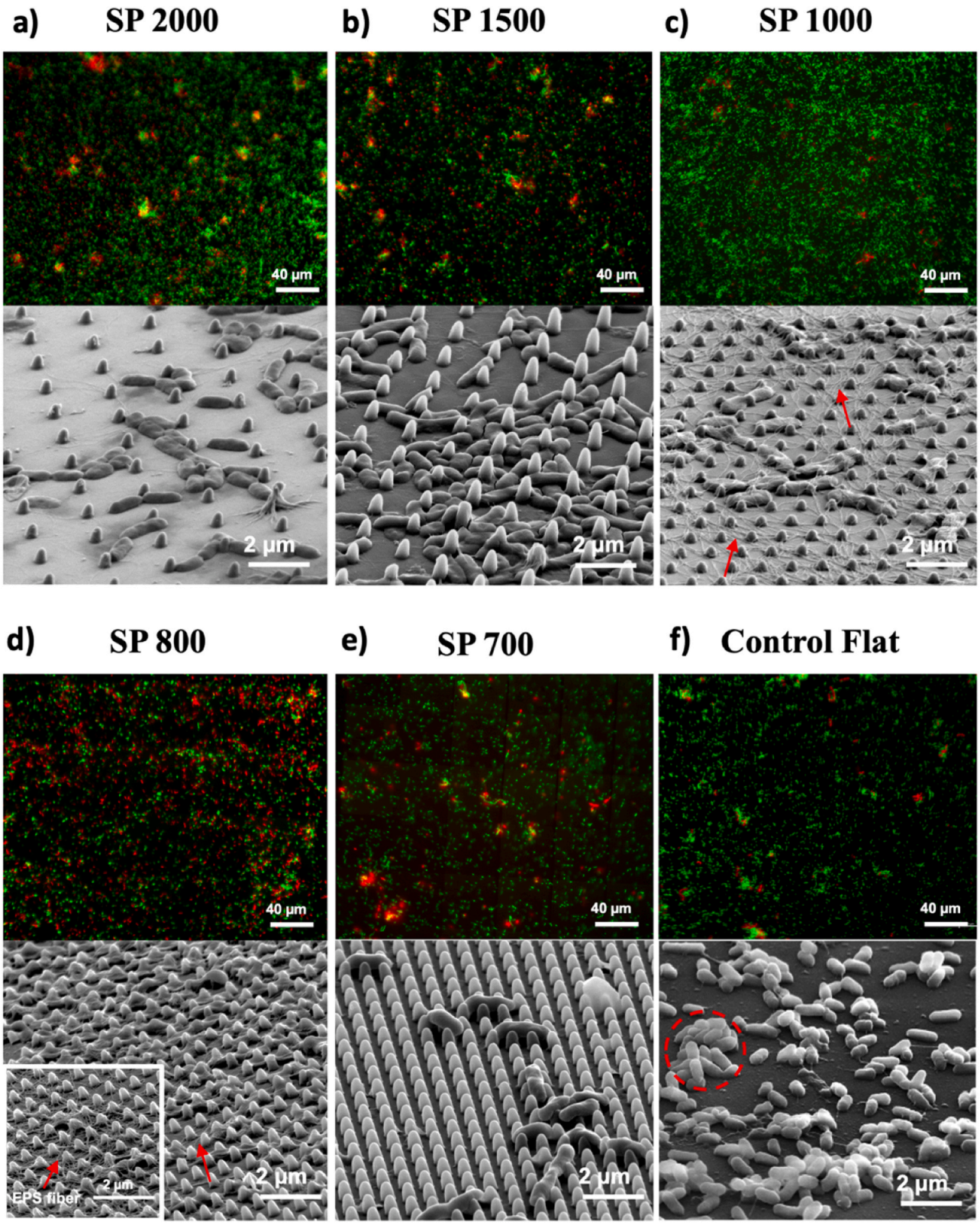

Fig. 4. Fluorescence micrographs (above) and corresponding SEM micrographs (below) of Pseudomonas aeruginosa after a 24-hour incubation period on nanopillar arrays (a): SP 2000, (b) SP 1500, (c) SP 1000, (d) SP 800, (e) SP 700, and (f) flat control. Note: The EPS fiber matrix surrounding SP 800 is shown as an inset in (d). Red arrows indicate the presence of EPS fiber matrix. The red dotted circle in (f) indicates initial aggregation of bacterial cells.

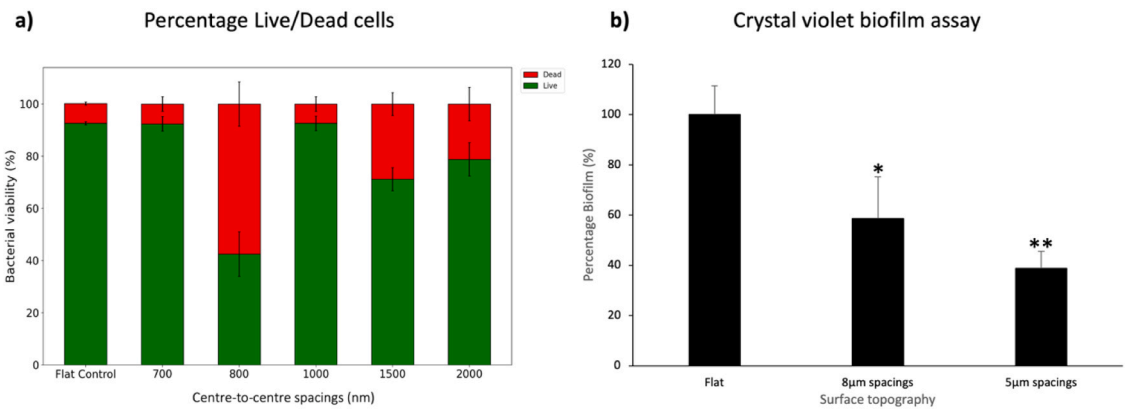

Fig. 5. (a) Bar chart illustrating the mean percentage of LIVE/DEAD bacteria, indicating the bactericidal performance of P. aeruginosa after 24 hr incubation on various nanopillared surfaces. (b) P. aeruginosa biofilm inhibition by micropillared surfaces. Bars represent the mean percentage biofilm ± s.d. of three independent replicates. * indicates statistical significance compared to flat control ($P < 0.05$, Student's t-test), and ** indicates statistical significance compared to flat control ($P < 0.01$, Student's t-test).

viable bacteria. In the corresponding SEM image, individual bacterial cells had aligned themselves between the interspaces of SP 1000 pillars accompanied by the presence of EPS webbing observed around the base of the nanopillar arrays. Surface-adhered bacterial cells produce EPS, crucial for biofilm formation and cellular attachment to surfaces, promoting higher proportions of bacteria cells [31].

In addition, all of the SEM images of nanopillar array samples, except for SP 800, displayed bacteria cells with turgid morphology, similar to those observed on flat control surfaces. In contrast, the cells observed in the SEM image of Fig. 4(d) when exposed to SP 800 exhibit deflation and leakage of their intracellular content, suggesting probable cell death. The LIVE/DEAD percentage results, shown in Fig. 5(a), corroborate the observations in Fig. 4. The closest spaced nanopillar array (SP 700) and SP 1000 demonstrated lowest dead cell count of 7.6 ± 2.8 % and 7.4 ± 2.8 %, respectively, similar to that of the control flat surface (7.6 ± 0.6 %), while nanopillar arrays in the SP 1500 and SP 2000 samples showed a higher bactericidal activity with a percentage dead cell count of 28.8 ± 6.2 % and 21.2 ± 6.4 %, respectively. Of note, the SP 800 sample showed the highest percentage of dead cell count at 57.5 ± 8.5 %.

Consequently, our study shows that nanopillar arrays of spacings 700 nm and 1000 nm demonstrated substantially lower bactericidal activity when compared to 1500 nm and 2000 nm spaced arrays, whereas the highest bactericidal activity was observed in 800 nm spaced pillars. It was hypothesized that the sparsely spaced pillars (i.e., SP 2000 and SP 1500) enabled the surface-adhered bacterial cells to move around, associated with the ripping effect. As the cells move and interact with the pillars, the friction produced would cause abrasions and eventually the effusion of cell content, and finally cell death [32]. These results are consistent with previous reports on prominent cell death in surface-adhered motile cells [12]. The observed differences in bacterial responses on SP 1000 and SP 800 samples highlight the contrasting effects of pillar spacings. As a result, the conformational arrangement of bacterial cells between the nanopillars in the SP1000 sample restricted the motility of the cells, thereby mitigating the abrasion effect and leaving most cells viable.

The minimal disruption of bacterial cells in closely spaced pillars (SP 700) corroborates with the SEM observation on cicada wing topography. Bacterial cells situated on the surface of the SP 700 sample remained intact (Fig. 4e). As described earlier, too closely spaced pillars (tip-to-tip adhesion) on certain areas of the cicada wings had resulted in decreased spacings between the tip-to-tip of the pillar groupings and increased in others. This causes an increase in localized surface area which is in contact with the bacteria, thereby limiting bacterium membrane stretching and reducing the killing effect. Likewise, reduced mechano-bactericidal activity of closely spaced SP 700 pillars is ascribed to the "bed-and-nails" effect. This effect is commonly interpreted as the uniform distribution of force across the bacterial cell, which renders membrane rupture more challenging. The SP 700 sample (with interspacing of ~367 nm) also had the least area coverage of *P. aeruginosa* on the nanopillared surface. Linklater et al. revealed that smaller and densely packed nanopillars on black silicon surface resulted in a decreased number of cell attachment [33]. As reported in previous studies, the anti-biofouling behaviour of microstructures was enhanced by having sufficiently dense interspacing (approximately 200 – 1000 nm) so that bacterial cells cannot fit in between the structures [34]. In the present work, the anti-biofouling effect was enhanced when the interspacing of the nanopillars was smaller than the minimum diameter of the *P. aeruginosa*, leaving most cells suspended above the nanopillars, minimizing the area of contact and adhesive force to the nanopillared surface.

A high proportion of EPS fiber matrix surrounding the SP 800 pillars as seen in the inset of scanning electron micrographs (Fig. 4d) may point to the stress factor exerted on the bacterial cells caused by the pillars [35]. The extracellular DNA found in the EPS acts as a cell-to-cell interconnecting compound within the biofilm matrix, it is also a complex defensive mechanism protecting bacteria from unfavourable environmental conditions. Indentations made by the nanopillar tips when the bacterial cell is suspended between the nanopillars place substantial stress on the bacterial cell membrane. The stress induced by nanopillars leads to the stiffening of the cell wall, causing a subsequent rise in turgor pressure. Cell rigidity was also another critical factor in determining the bacteria cells' susceptibility to mechanical rupture [36]. Exceeding the stretching degree threshold of the membrane elastic layer would generate localized stress on bacterial cell membranes, leading to mechanical rupture and loss in internal turgor pressure. This would result in the effusion of cell contents and changes in morphology, ultimately leading to rapid cell death [23,31,32]. With great precision and controllability of the nanopillar array, the mechano-bactericidal action of the two-photon polymerized SP800 nanopillar array was consistent throughout, unlike the inhomogeneous nano-architecture on cicada wings which resulted in the uneven distribution of the mechano-bactericidal activity. However, despite having the greatest bactericidal activity in SP800, a significant amount of bacterial cell debris remained attached to the surface as seen in the fluorescence micrograph of Fig. 4(d).

It is therefore important to study the release of bacteria debris killed by the nanostructured surfaces, possibly through the integration of microtopographical surfaces, as the accumulation of bacterial debris on the surface may compromise the killing efficacy of nano-pillar arrays

over time. Bacterial debris containing nutrients would provide an anchoring point for bacterial proliferation and subsequent biofilm formation [34,35]. Notably, bacterial cells on a flat control surface showed several clusters of bacterial microcolonies, possibly indicating the initial stages of biofilm formation (Fig. 4f) [37], while this phenomenon was not apparent in the 2PP nanopillared surfaces.

3.4.2. Effect of nanopillar aspect ratio on antimicrobial activity

Overall, nanofeatures with an aspect ratio between 0.56 and 0.83 (as listed in Table 1) were fabricated in this work, but no correlation was found between the bactericidal efficacy and aspect ratio. With a similar aspect ratio of 0.61 (SP 700) and 0.64 (SP 800), the percentage of dead *P. aeruginosa* cells adhered on the surface was 7.6 % and 57.5 %, respectively. While nanofeatures with aspect ratio values of 0.61 (SP 700) and 0.83 (SP 1000) with $>$ 36 % variability showed a similar percentage (~7 %) of adherent dead cells. Similarly, no correlation between aspect ratio and bacteria killing effect was reported by Gavin et. al [25], who fabricated independent poly(ethylene terephthalate) nanocone arrays with centre-to-centre spacings of 500 nm and 200 nm. The 500 nm spaced arrays, with an aspect ratio ranging from 0.37 to 0.61, showed no significant differences ($P > 0.05$) in the percentage of attached dead *K. pneumoniae* (~15 % stained dead cells) on each of their surfaces, despite having a variability of $>$ 64 % in aspect ratio. In contrast, the 200 nm spaced nanocone array, with an aspect ratio of 0.33, showed over 26 % stained dead *K. pneumoniae*. This observation reinforces the solid influence of nanofeature spacings on bactericidal efficacy. As reviewed by Ishantha Senevirathne et. al [38], previous studies found no correlation for gram-negative bacteria, while only a weak positive correlation (r=0.28) was found for Gram-positive bacteria.

3.4.3. Effect of spacings in micropillar arrays on biofilm inhibition

The biofilm inhibition activity of micropillar arrays with 5 μm and 8 μm centre-to-centre spacings was compared to the flat surface through a static biofilm assay using crystal violet dye. The dye, which adheres to surface-associated biofilm mass, results in a higher optical density value in samples with a greater quantity of bacterial biofilm mass attachment. Following a 24-hour incubation period, the micropillared topography effectively hindered the attachment of *P. aeruginosa* biofilm, compared to the flat control surface, as shown in Fig. 5(b). There is a 41 % decrease in biofilm formation for the microtopography with 8 μm centre-to-centre spacings, whereas the sample with 5 μm centre-to-centre spacings exhibited 61 % statistically significant (P value < 0.01) reduction in biofilm formation with respect to the control flat surface. This sample had an interspace of ~ 2 μm distance between nearest pillars, similar to the typical dimension of *P. aeruginosa* bacterial cell which measures around 1.5 μm to 3 μm in length [39]. The micropillar spacings in 8 μm topography were much greater (~ 5 μm interspacing) than the dimensions of *P. aeruginosa* cell. When a bacterium lands on a surface with micropillars, there is a decrease in localized stress and contact pressure exerted on bacterial cells compared to nanopillars. This is due to the increased contact area between the cell and the pillar wall surface, which is insufficient to cause significant membrane deformation. Therefore, micropillars merely exhibit an anti-biofouling activity. The higher antibiofouling activity of the 2PP microstructures (5 μm spaced micropillars) was in corroboration with previous studies in which microscale or nanoscale surface structures are capable of resisting fouling agents (i.e., bacteria, algal spores, or yeast) that are in similar length scales to the surface topographies [40]. In addition, previous published work on the biomimetic cylinder-based microstructures (diameter of 3 μm and height of 3 μm) of crabs exhibited antifouling release performance against *Phaeodactylum tricornutum* which is 2–3 μm wide [41]. Another study showed that poly(dimethyl siloxane) elastomer surfaces, a replica of the Sharklet AF™ design, with a height of 3 μm and 2 μm interspacing between neighbouring rectangular ribs of varying lengths ranging from 4 to 16 μm exhibited an inhibitory effect on *S. aureus* (0.5 – 1 μm diameter) biofilm colonization over the course of 21 days despite the absence of bactericidal agents [14].

3.5. Transcriptomic analysis of bacterial cell exposed to 2PP nanopillared and flat surfaces

Finally, we investigated the effects of SP 800 nanopillared array on *P. aeruginosa* gene expression by utilizing a comprehensive whole transcriptome sequencing approach. A total of 7 out of 5653 genes were found to be significantly differentially expressed in *P. aeruginosa* exposed to the SP 800 nanopillared surface (fold change > 2, adjusted $P < 0.05$, Table 2). The gene expression values were compared between sample group types, $\log_2$FoldChange indicates how much the gene expression has changed due to exposure to 2PP nanopillared surfaces compared to control flat samples. PA3305.1 (*phrS*) and PA4690.5 were found to be significantly up-regulated, while PA0668.4, PA4690.2, PA0668.5, PA4726.2 and PA4421.1 (*rnpB*) were significantly down-regulated in SP 800 samples (Fig. 6).

Further pathway analysis using Kyoto Encyclopedia of Genes and Genomes (KEGG) database identified a single pathway associated with quorum sensing was significantly enriched. Indeed, PA3305.1 (PhrS) which was significantly up-regulated in *P. aeruginosa* following exposure to SP 800 nanopillar, is known to be an inducer of quinolone signal synthesis [42,43]. Quinolone signal synthesis increases the production of reactive oxygen species (ROS), which exposes the bacteria to oxidative stress and cell death by disrupting cell membrane integrity [44–46]. Overall, these results suggest that SP 800 nanopillared array may induce bacteria cell death through upregulation of *PhrS* and quorum sensing signalling.

4. Conclusion

In conclusion, 2PP technique was used in this study to produce well-controlled and precise uniform, nanopillar and micropillar arrays on glass substrates to study the antibacterial effect of these geometries on the Gram-negative *P. aeruginosa*, without the use of chemical antimicrobial agents. Surface configurations featuring hexagonally arranged pillars with 500 nm interspacing such as those from SP 800 nanopillar array, have demonstrated the greatest bactericidal efficacy compared to those with closer or wider spacings, suggesting that the effectiveness of

Table 2
List of significant differentially regulated genes (DEG) following exposure to SP800 nanopillar in P. aeruginosa.

Gene Name	RNA Name	Log_2 Fold-Change	pvalue	padj
PA4690.5	16 S ribosomal RNA	5.53	1.06E-02	3.86E-02
PA3305.1	other	3.02	6.72E-30	2.69E-28
PA4421.1	RNase_P_RNA	-1.08	6.70E-06	4.47E-05
PA4726.2	other	-1.48	2.83E-06	2.27E-05
PA4690.2	23 S ribosomal RNA	-1.69	3.39E-09	4.52E-08
PA0668.4	23 S ribosomal RNA	-1.71	1.75E-09	3.49E-08
PA0668.5	5 S ribosomal RNA	-2.07	1.53E-07	1.53E-06

NOTE: DEG is defined as gene expression with fold-change > 2 and padj < 0.05. The padj indicates adjusted p values which satisfy the property of thresholding at a specific value defined by a set of tests (one for each gene) with a bounded false discovery rate (FDR).

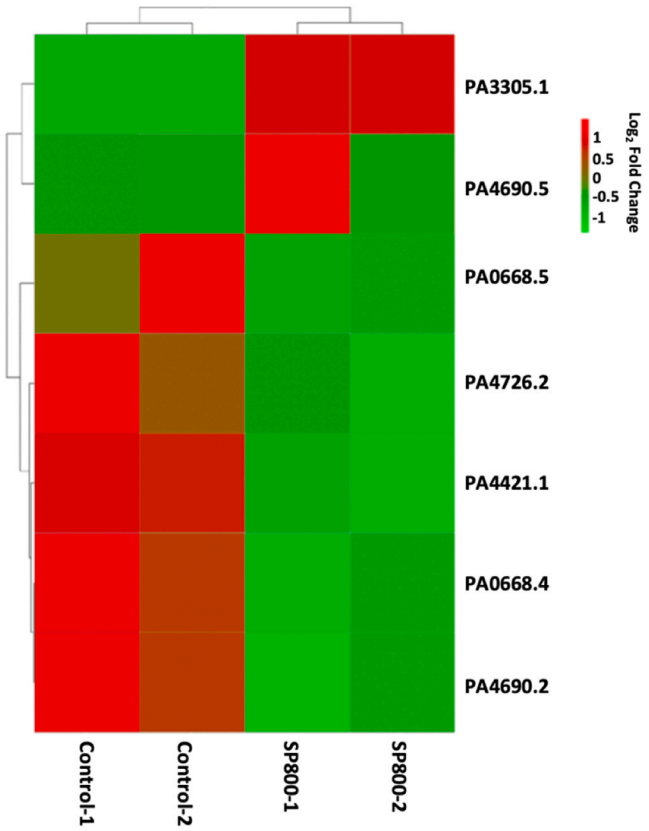

Fig. 6. Heatmap representing the 7 significant differentially expressed genes (DEGs) following exposure to SP 800 nanopillared surfaces vs control. The lines on the left side of the heatmap represent the hierarchical clustering of the genes based on their expression profiles across the samples. This clustering groups genes with similar expression patterns, indicating potential relatedness in their functional roles or regulation mechanisms. The lines at the top of the heatmap represent hierarchical clustering of the samples, indicating similarities and differences in overall gene expression patterns between the different conditions. Note that the clustering reveals that Control-1 and Control-2 samples cluster together, and similarly, SP800–1 and SP800–2 samples also cluster together, suggesting a similarity in gene expression induced by SP 800 across two independent experiments.

nanopillar arrays in interacting with bacterial cells depends on the spatial arrangement of the pillars relative to the size of the bacteria. Whole transcriptomic analysis of *P. aeruginosa* exposed to SP 800 revealed potential alterations in their quorum sensing pathway. Furthermore, micropillar arrays demonstrated biofilm-inhibitive properties. Micropillars arranged in hexagonal pattern with 2 μm interspacing, approximately the size of bacterial cells, displayed significant biofilm inhibition properties.

To address the challenges of accumulating surface-killed bacteria, preventing biofilm formation, and maintaining long-term antibacterial effects, further research is necessary to optimally combine these nanostructures and microstructures. Such integration could significantly enhance antibacterial efficacy by synergizing their respective properties. Future research exploring other aspects including feature shape, surface wettability, and variability of the bacterial characteristics could provide deeper insights into optimising mechano-antibacterial surfaces to suit potential applications across various industries and healthcare settings.

On a final note, although the precision and controllability of the 2PP technique are well established at the laboratory scale, its use in industrial-level, high-volume production is constrained by its small patternable micron-size array and slow writing speed. However, future advancements in rapid replication molding using 2PP prototypes may overcome these limitations, enabling large scale production.

CRediT authorship contribution statement

Chee-Onn Leong: Resources, Methodology. **Ricky D. Wildman:** Supervision, Resources. **Nigel Neate:** Investigation. **Ning Tan:** Writing – original draft, Visualization, Software, Methodology, Investigation, Formal analysis, Conceptualization. **Jisun Im:** Investigation. **Georgina Elizabeth Marsh:** Writing – review & editing, Validation, Supervision, Conceptualization. **Maxine Swee-Li Yee:** Writing – review & editing, Visualization, Supervision, Project administration, Funding acquisition, Conceptualization.

Declaration of Competing Interest

The authors declare that they have no known competing financial interests or personal relationships that could have appeared to influence the work reported in this paper.

Data availability

Data will be made available on request.

Acknowledgements

This research was funded by Ministry of Higher Education Malaysia FRGS/1/2020/TK0/UNIM/03/3 and UNM FOSE internal grant LA744019.

References

[1] M. Jamal, W. Ahmad, S. Andleeb, F. Jalil, M. Imran, M.A. Nawaz, T. Hussain, M. Ali, M. Rafiq, M.A. Kamil, Bacterial biofilm and associated infections, J. Chin. Med. Assoc. (2018), https://doi.org/10.1016/j.jcma.2017.07.012.
[2] M.H. Muhammad, A.L. Idris, X. Fan, Y. Guo, Y. Yu, X. Jin, J. Qiu, X. Guan, T. Huang, Beyond risk: bacterial biofilms and their regulating approaches, Front. Microbiol. (2020), https://doi.org/10.3389/fmicb.2020.00928.
[3] T.F. Mah, Biofilm-specific antibiotic resistance, Future Microbiol (2012), https://doi.org/10.2217/fmb.12.76.
[4] Hip and knee replacement, in: OECD Publishing, Paris, 2021. https://doi.org/10.1787/8b492d7a-en.
[5] P. Izakovicova, O. Borens, A. Trampuz, Periprosthetic joint infection: current concepts and outlook, EFORT Open Rev. 4 (2019), https://doi.org/10.1302/2058-5241.4.180092.
[6] L.K. Vestby, T. Grønseth, R. Simm, L.L. Nesse, Bacterial biofilm and its role in the pathogenesis of disease, Antibiotics 9 (2020), https://doi.org/10.3390/antibiotics9020059.
[7] C.M. Mallon, R. Gooberman-Hill, A.J. Moore, Infection after knee replacement: a qualitative study of impact of periprosthetic knee infection, BMC Musculoskelet. Disord. 19 (2018), https://doi.org/10.1186/s12891-018-2264-7.
[8] R.O. Darouiche, Treatment of infections associated with surgical implants, N. Engl. J. Med. 350 (2004), https://doi.org/10.1056/nejmra035415.
[9] A. Gallardo-Godoy, C. Muldoon, B. Becker, A.G. Elliott, L.H. Lash, J.X. Huang, M. S. Butler, R. Pelingon, A.M. Kavanagh, S. Ramu, W. Phetsang, M.A.T. Blaskovich, M.A. Cooper, Activity and predicted nephrotoxicity of synthetic antibiotics based on polymyxin B, J. Med. Chem. (2016), https://doi.org/10.1021/acs.jmedchem.5b01593.
[10] K. Modaresifar, S. Azizian, M. Ganjian, L.E. Fratila-Apachitei, A.A. Zadpoor, Bactericidal effects of nanopatterns: a systematic review, Acta Biomater. (2019), https://doi.org/10.1016/j.actbio.2018.09.059.
[11] S.M. Kelleher, O. Habimana, J. Lawler, B. O'reilly, S. Daniels, E. Casey, A. Cowley, Cicada wing surface topography: an investigation into the bactericidal properties of nanostructural features, ACS Appl. Mater. Interfaces 8 (2016), https://doi.org/10.1021/acsami.5b08309.
[12] C.D. Bandara, S. Singh, I.O. Afara, A. Wolff, T. Tesfamichael, K. Ostrikov, A. Oloyede, Bactericidal effects of natural nanotopography of dragonfly wing on escherichia coli, ACS Appl. Mater. Interfaces 9 (2017), https://doi.org/10.1021/acsami.6b13666.
[13] J. Román-Kustas, J.B. Hoffman, J.H. Reed, A.E. Gonsalves, J. Oh, L. Li, S. Hong, K. D. Jo, C.E. Dana, N. Miljkovic, D.M. Cropek, M. Alleyne, Molecular and topographical organization: influence on cicada wing wettability and bactericidal properties, Adv. Mater. Interfaces 7 (2020), https://doi.org/10.1002/admi.202000112.
[14] K.K. Chung, J.F. Schumacher, E.M. Sampson, R.A. Burne, P.J. Antonelli, A. B. Brennan, Impact of engineered surface microtopography on biofilm formation of

Staphylococcus aureus, Biointerphases 2 (2007), https://doi.org/10.1116/1.2751405.
[15] S. Nir, M. Reches, Bio-inspired antifouling approaches: the quest towards non-toxic and non-biocidal materials, Curr. Opin. Biotechnol. 39 (2016), https://doi.org/10.1016/j.copbio.2015.12.012.
[16] A.K. Epstein, T.S. Wong, R.A. Belisle, E.M. Boggs, J. Aizenberg, Liquid-infused structured surfaces with exceptional anti-biofouling performance, Proc. Natl. Acad. Sci. U. S. A. 109 (2012), https://doi.org/10.1073/pnas.1201973109.
[17] F. Jipa, M. Zamfirescu, A. Velea, M. Popescu, R. Dabu, Femtosecond laser lithography in organic and non-organic materials, Updat. Adv. Lithogr. (2013), https://doi.org/10.5772/56579.
[18] M. Emons, K. Obata, T. Binhammer, A. Ovsianikov, B.N. Chichkov, U. Morgner, Two-photon polymerization technique with sub-50 nm resolution by sub-10 fs laser pulses, Opt. Mater. Express (2012), https://doi.org/10.1364/ome.2.000942.
[19] X. Zhou, Y. Hou, J. Lin, A review on the processing accuracy of two-photon polymerization, AIP Adv. (2015), https://doi.org/10.1063/1.4916886.
[20] N. Tan, J. Im, N. Neate, R.D. Wildman, G.E. Marsh, M.S.L. Yee, Revolutionizing antibacterial surfaces: 3D printed nanoscale and microscale topographies through two-photon polymerization, Key Eng. Mater. 977 (2024) 163–172, https://doi.org/10.4028/p-9mqipb.
[21] B.P. Kamarajan, A. Muthusamy, Survival strategy of Pseudomonas aeruginosa on the nanopillar topography of dragonfly (Pantala flavescens) wing, AMB Express 10 (2020), https://doi.org/10.1186/s13568-020-01021-7.
[22] F. Xue, J. Liu, L. Guo, L. Zhang, Q. Li, Theoretical study on the bactericidal nature of nanopatterned surfaces, J. Theor. Biol. 385 (2015), https://doi.org/10.1016/j.jtbi.2015.08.011.
[23] S. Wu, F. Zuber, K. Maniura-Weber, J. Brugger, Q. Ren, Nanostructured surface topographies have an effect on bactericidal activity, J. Nanobiotechnol. (2018), https://doi.org/10.1186/s12951-018-0347-0.
[24] M.N. Dickson, E.I. Liang, L.A. Rodriguez, N. Vollereaux, A.F. Yee, Nanopatterned polymer surfaces with bactericidal properties, Biointerphases (2015), https://doi.org/10.1116/1.4922157.
[25] G. Hazell, L.E. Fisher, W.A. Murray, A.H. Nobbs, B. Su, Bioinspired bactericidal surfaces with polymer nanocone arrays, J. Colloid Interface Sci. 528 (2018), https://doi.org/10.1016/j.jcis.2018.05.096.
[26] E.P. Ivanova, J. Hasan, H.K. Webb, V.K. Truong, G.S. Watson, J.A. Watson, V. A. Baulin, S. Pogodin, J.Y. Wang, M.J. Tobin, C. Löbbe, R.J. Crawford, Natural bactericidal surfaces: mechanical rupture of pseudomonas aeruginosa cells by cicada wings, Small 8 (2012), https://doi.org/10.1002/smll.201200528.
[27] M. Ganjian, K. Modaresifar, M.R.O. Ligeon, L.B. Kunkels, N. Tümer, L. Angeloni, C. W. Hagen, L.G. Otten, P.L. Hagedoorn, I. Apachitei, L.E. Fratila-Apachitei, A. A. Zadpoor, Nature helps: toward bioinspired bactericidal nanopatterns, Adv. Mater. Interfaces 6 (2019), https://doi.org/10.1002/admi.201900640.
[28] M. Rohde, The gram-positive bacterial cell wall, Microbiol. Spectr. 7 (2019), https://doi.org/10.1128/microbiolspec.gpp3-0044-2018.
[29] S.P. Diggle, M. Whiteley, Microbe profile: pseudomonas aeruginosa: opportunistic pathogen and lab rat, Microbiol. 166 (2020), https://doi.org/10.1099/mic.0.000860.
[30] A. Velic, A. Jaggessar, T. Tesfamichael, Z. Li, P.K.D.V. Yarlagadda, Effects of nanopillar size and spacing on mechanical perturbation and bactericidal killing efficiency, Nanomaterials (2021), https://doi.org/10.3390/nano11102472.
[31] M.T.T. Thi, D. Wibowo, B.H.A. Rehm, Pseudomonas aeruginosa biofilms, Int. J. Mol. Sci. 21 (2020), https://doi.org/10.3390/ijms21228671.
[32] K. Jindai, K. Nakade, K. Masuda, T. Sagawa, H. Kojima, T. Shimizu, S. Shingubara, T. Ito, Adhesion and bactericidal properties of nanostructured surfaces dependent on bacterial motility, RSC Adv. 10 (2020), https://doi.org/10.1039/c9ra08282d.
[33] D.P. Linklater, H.K.D. Nguyen, C.M. Bhadra, S. Juodkazis, E.P. Ivanova, Influence of nanoscale topology on bactericidal efficiency of black silicon surfaces, Nanotechnology 28 (2017), https://doi.org/10.1088/1361-6528/aa700e.
[34] N. Encinas, C.Y. Yang, F. Geyer, A. Kaltbeitzel, P. Baumli, J. Reinholz, V. Mailänder, H.J. Butt, D. Vollmer, Submicrometer-sized roughness suppresses bacteria adhesion, ACS Appl. Mater. Interfaces (2020), https://doi.org/10.1021/acsami.9b22621.
[35] H. Mulcahy, L. Charron-Mazenod, S. Lewenza, Pseudomonas aeruginosa produces an extracellular deoxyribonuclease that is required for utilization of DNA as a nutrient source, Environ. Microbiol. 12 (2010), https://doi.org/10.1111/j.1462-2920.2010.02208.x.
[36] S. Pogodin, J. Hasan, V.A. Baulin, H.K. Webb, V.K. Truong, T.H. Phong Nguyen, V. Boshkovikj, C.J. Fluke, G.S. Watson, J.A. Watson, R.J. Crawford, E.P. Ivanova, Biophysical model of bacterial cell interactions with nanopatterned cicada wing surfaces, Biophys. J. 104 (2013), https://doi.org/10.1016/j.bpj.2012.12.046.
[37] H.C. Flemming, J. Wingender, U. Szewzyk, P. Steinberg, S.A. Rice, S. Kjelleberg, Biofilms: an emergent form of bacterial life, Nat. Rev. Microbiol. 14 (2016), https://doi.org/10.1038/nrmicro.2016.94.
[38] S.W.M.A. Ishantha Senevirathne, J. Hasan, A. Mathew, A. Jaggessar, P.K.D. V. Yarlagadda, Trends in bactericidal nanostructured surfaces: an analytical perspective, ACS Appl. Biol. Mater. 4 (2021), https://doi.org/10.1021/acsabm.1c00839.
[39] S. Baron, Medical Microbiology. 4th edition, 1996.
[40] J. Hasan, S. Jain, R. Padmarajan, S. Purighalla, V.K. Sambandamurthy, K. Chatterjee, Multi-scale surface topography to minimize adherence and viability of nosocomial drug-resistant bacteria, Mater. Des. (2018), https://doi.org/10.1016/j.matdes.2017.11.074.
[41] Z. Yang, X. Bai, X. He, C. Yuan, Study on biomimetic antifouling surface preparation based on surface microstructure of crabs, ICTIS 2019 5th Int. Conf. Transp. Inf. Saf. (2019), https://doi.org/10.1109/ICTIS.2019.8883729.
[42] S.Y.Y. Tan, Y. Liu, S.L. Chua, R.M. Vejborg, T.H. Jakobsen, S.C. Chew, Y. Li, T. E. Nielsen, T. Tolker-Nielsen, L. Yang, M. Givskov, Comparative systems biology analysis to study the mode of action of the isothiocyanate compound iberin on Pseudomonas aeruginosa, Antimicrob. Agents Chemother. 58 (2014), https://doi.org/10.1128/AAC.02620-13.
[43] E. Sonnleitner, N. Gonzalez, T. Sorger-Domenigg, S. Heeb, A.S. Richter, R. Backofen, P. Williams, A. Hüttenhofer, D. Haas, U. Bläsi, The small RNA PhrS stimulates synthesis of the Pseudomonas aeruginosa quinolone signal, Mol. Microbiol. 80 (2011), https://doi.org/10.1111/j.1365-2958.2011.07620.x.
[44] R. Bright, D. Fernandes, J. Wood, D. Palms, A. Burzava, N. Ninan, T. Brown, D. Barker, K. Vasilev, Long-term antibacterial properties of a nanostructured titanium alloy surface: an in vitro study, Mater. Today Biol. 13 (2022), https://doi.org/10.1016/j.mtbio.2021.100176.
[45] L. Yang, K.B. Barken, M.E. Skindersoe, A.B. Christensen, M. Givskov, T. Tolker-Nielsen, Effects of iron on DNA release and biofilm development by Pseudomonas aeruginosa, Microbiology 153 (2007), https://doi.org/10.1099/mic.0.2006/004911-0.
[46] B. Tettmann, C. Niewerth, F. Kirschhöfer, A. Neidig, A. Dötsch, G. Brenner-Weiss, S. Fetzner, J. Overhage, Enzyme-mediated quenching of the pseudomonas quinolone signal (PQS) promotes biofilm formation of pseudomonas aeruginosa by increasing iron availability, Front. Microbiol. 7 (2016), https://doi.org/10.3389/fmicb.2016.01978.